arXiv:1212.4841v1 [cond-mat.other] 19 Dec 2012

# Understanding quantum decoherence pathways using time-resolved spectroscopy

Michael Sentef,[1] Alexander F. Kemper,[2] Brian Moritz,[1,3,4] James K. Freericks,[5] Zhi-Xun Shen,[1,6,7] and Thomas P. Devereaux[1,7]

[1]*Stanford Institute for Materials and Energy Sciences (SIMES),*
*SLAC National Accelerator Laboratory, Menlo Park, CA 94025, USA*
[2]*Lawrence Berkeley National Lab, 1 Cyclotron Road, Berkeley, CA 94720, USA*
[3]*Department of Physics and Astrophysics,*
*University of North Dakota, Grand Forks, ND 58202, USA*
[4]*Department of Physics, Northern Illinois University, DeKalb, IL 60115, USA*
[5]*Department of Physics, Georgetown University, Washington, DC 20057, USA*
[6]*Departments of Physics and Applied Physics,*
*Stanford University, Stanford, California 94305, USA*
[7]*Geballe Laboratory for Advanced Materials,*
*Stanford University, Stanford, CA 94305*

## Abstract

In condensed matter physics, nonequilibrium pump-probe time domain spectroscopies have become an important tool to disentangle degrees of freedom whose coupling leads to broad structures in the frequency domain. Here, using the time-resolved solution of a model photoexcited electron-phonon system we show that the relaxational dynamics are governed by the *equilibrium* self-energy so that the phonon frequency sets a window for "slow" versus "fast" recovery. The overall temporal structure of this relaxation spectroscopy allows for a reliable and quantitative extraction of the electron-phonon coupling strength without resorting to an effective temperature model.

In pump-probe experiments, phonons provide the primary channel for photoexcited electrons to relax and reduce their energy via scattering. By emitting phonons, the electrons dissipate the excess energy imparted by the photons, eventually reaching a new thermal equilibrium. The rate at which electrons can dissipate their energy is determined, in part, by the strength of electron-phonon coupling. This coupling is also of critical importance in determining other properties of a material, such as electrical or thermal transport, the effective electronic mass enhancement, the size of the polaronic cloud that surrounds an electron in the normal state, or the superconducting properties of a BCS superconductor. As with many basic coupling constants in nature, it is difficult to directly measure the strength of electron-phonon coupling, making it a challenge to assess its role in materials like high temperature superconductors. Here we show how one can measure the electron-phonon coupling from relaxational pump-probe photoemission spectroscopy.

The strength of electron-phonon coupling is commonly described through one of two dimensionless coupling constants: $\lambda$ determines the change in the electronic specific heat due to electron-phonon coupling, the renormalization of the Fermi liquid properties due to phonons, and the superconducting properties, while the transport coupling strength $\lambda_{tr}$ determines transport properties. In conventional superconductors, an inversion[1] of the fine structure in the tunneling density of states above the gap can be used to determine $\lambda$ to high precision. The transport coupling strength $\lambda_{tr}$ can be found by inverting optical conductivity data,[2,3] even in the normal state.[4] In both cases, the phonon effects must be dominant and strong for the inversion to be accurate. Other experimental methods of determining electron-phonon couplings include x-ray scattering,[5] Raman scattering,[6] or neutron scattering.[7]

Angle-resolved photoemission (ARPES) has been widely used to determine the low-energy electronic structure of a variety of materials.[8,9] Many-body interaction effects are manifest via the self energy $\Sigma$ giving rise to renormalizations of the electron mass and an overall broadening of the spectral function. As an example, it was thought that ARPES data for the cuprates could thereby be studied to extract the boson coupling that is responsible for high temperature superconductivity.[10–26] These investigations have provided important insights into the underlying bosons and interactions responsible for kinks in the electronic dispersion. However, extracting the self-energy and a meaningful coupling constant from frequency-dependent ARPES data can be challenging, especially when many sources of incoherence are present simultaneously.

As an alternative, a time domain approach using the relaxation of excited electrons back to equilibrium as a direct technique to measure electron-phonon coupling was proposed by Allen.[27] The basic quantities for this method are the deviations from the initial equilibrium values of the electron and phonon occupations in momentum space. A semi-classical Boltzmann approximation that averages over momenta was used to extract estimates for electron-phonon couplings from pump-probe photoemission data in simple elemental metals.[28,29] It also was applied to high-temperature superconductors[30–33] even though the approximation can be justified at best for simple Drude metals subject to relatively weak driving fields in the linear response regime.

However, in more correlated materials, such as transition metal oxides like the cuprates, or in multiband systems with multiple disconnected Fermi surface pieces, such as the iron pnictides, the momentum dependence must be resolved, since it is a crucial ingredient for these materials' interesting properties.[34,35] In addition, a full quantum mechanical formulation is required to treat arbitrarily strong fields and strong energy and momentum dependent scattering, particularly in materials where the balance between various competing phases may be tipped with the application of strong electric fields. Examples include possible light-induced superconductivity in a stripe-ordered cuprate,[36] a dramatically enhanced conductivity in an oxide heterostructure.[37], coherent phonon oscillations serving as a marker for a photoinduced phase transition in $VO_2$,[38], and pump-probe photoemission providing a novel classification scheme for charge-density wave insulators in the time domain.[39]

In this paper we present a microscopic quantum nonequilibrium approach with full momentum and energy resolution that can be applied when the semiclassical Boltzmann equation fails, and can be used in conjunction with standard many-body and material specific computational approaches. Using our model system, we show how the time ($t$), momentum ($\boldsymbol{k}$), and energy ($\omega$) resolution provided by state-of-the-art tr-ARPES[30–33,40–45] experiments in conjunction with the dependence of extracted decay times on the initial equilibrium sample temperature provides a direct method to measure the dominant phonon energy and electron-phonon coupling. Hence, we show that relaxational spectroscopy in the time domain allows the possibility to extract detailed information about the system *in equilibrium* and lend itself to a simple interpretation beyond the traditional two-temperature model phenomenology.

# I. RESULTS

## A. Photoexcited electronic structure: Energy and temperature dependent relaxation

We consider 2D tight binding electrons in a single partially filled metallic band coupled to the lattice via electron-phonon coupling in a Holstein model[46] (see Supplementary Material). Phonons are described by a single optical branch with momentum-independent phonon frequency $\Omega = 0.1$ eV and electron-phonon coupling $g = \sqrt{0.02}$ eV as representative values for optical phonons in transition metal oxides. Our approach can be generalized to momentum-dependent phonons and momentum-dependent couplings. In equilibrium, the phonon frequency sets the relevant energy scale at which a kink at $\pm\Omega$ in the band structure occurs[47], as shown in Figure 1a-c. The dimensionless coupling constant $\lambda$ is a measure of the strength of lattice distortion relative to the kinetic energy of the electrons. $\lambda$ is defined via the slope of the real part of the self-energy and determines the electronic mass renormalization. Our choice of parameters corresponds to a value of $\lambda = 0.42$. This value of $\lambda$ is sufficiently large to produce a kink in the dispersion, but still small enough to justify the use of the Migdal approximation for the electron-phonon coupling (see Supplement).

The system is prepared in an initial equilibrium state at a temperature $T$. Subsequently the electrons are photoexcited by a pump laser pulse modeled by a time-dependent electric field. We utilize the Keldysh technique for calculating the electron propagation along the Keldysh contour (see Supplement for details). The electric field of the pump pulse is included via a Peierls substitution valid for any temporal field shape or strength. This approach has been formulated earlier by Jauho and Wilkins[48] which we extend numerically to longer time scales and arbitrary field strengths. Specifically we choose a Gaussian field envelope of width $\sigma = 25$ femtoseconds (fs) and a frequency of 0.5 eV, as representative of a typical pump setup. The delay time is defined with respect to the center of the Gaussian pulse envelope. The electric field is linearly polarized along the Brillouin zone diagonal (see inset in Figure 1a and Supplement). We have checked in the analysis of the transient relaxation that details of the pump are not especially important unless there is a competing phase to which we can pump,[36,49] and unless we are interested in the behavior during the pump. The subsequent tr-ARPES probe pulse has a Gaussian envelope width of $\sigma_{pr} = 103$ fs. In the Supplement, we also show the equilibrium tr-ARPES spectra for smaller $\sigma_{pr}$, which enables a better time resolution but necessarily leads to worse energy resolution.

In Figure 1 we show the energy- and momentum-resolved tr-ARPES spectra along a nodal cut for three delay times before (1a), during (1b), and after the pump pulse (1c). The pump pulse drives electrons from below the Fermi level $E_F$ to empty states above $E_F$ (Figure 1b) as the system absorbs energy leaving the electrons in a photoexcited state. The excess energy of the electrons is then transferred into the bath of phonons, and the electrons relax back towards equilibrium (Figure 1c). Figure 1d provides a comparison of the $\boldsymbol{k}$-resolved energy distribution curves (EDC) before and 558 fs after the pump. Clearly, the phonon window $\mathcal{W} = [-\Omega, \Omega]$ around the Fermi level sets an energy scale for persistent spectral changes: while electronic quasiparticles outside this window have already relaxed back to their equilibrium EDC, the quasiparticles inside remain excited at the particular time delay shown here. This phonon window effect is highlighted in the momentum-integrated pump-induced spectral changes in Figure 1e: photoexcited electrons above $E_F$ and holes below $E_F$ only persist inside the window set by the phonon frequency $\Omega$.

In equilibrium at zero temperature, kinematics prevents electron relaxation unless the quasiparticles have sufficient energy to emit phonons, which is why this window is not unexpected. In Figure 1f, we show that raising the initial equilibrium temperature leads to smaller spectral changes compared to Figure 1d at the same time delay. Correspondingly, the $\boldsymbol{k}$-integrated spectral changes shown in Figure 1g are significantly smaller than the ones in 1e (shown on the same vertical scale), although the phonon window effect is still visible.

A simple way of thinking about pump-probe experiments has been that pumping the system is approximately the same as heating. Models of “hot electrons” assume that the laser pump initially raises the electronic temperature.[27,50] The electrons then transfer their excess energy to the lattice until the electronic and lattice subsystems equilibrate. Here, the hot electron picture does not provide a valid description of the photoexcited electrons in our system, which is demonstrated in Figure 2.

In Figure 2a and 2b, we show the momentum-resolved tr-ARPES spectrum along the diagonal momentum cut at a short time delay (4 fs) for two different pump pulses. Figure 2a is for the same maximum field strength $E_{\max} = 0.4$ V$/a_0$ that was used in Figure 1; Figure 2b is for a ten times stronger field. The weaker pump mainly excites electrons within the bare energy band, but the stronger pump clearly disrupts the band structure and induces ladder-like structures which are reminiscent of Wannier-Stark ladders in strong dc electric fields.[51,52]

The breakdown of the "hot electron" picture becomes more evident when we integrate the tr-ARPES spectra in the momentum window around the Fermi momentum between $\boldsymbol{k}_1$ and $\boldsymbol{k}_7$ (see Figure 1). The energy distribution curves in Figure 2c are not simply featureless decaying exponentials, as they would be if the "hot electron" model was valid, but show distinct higher energy peaks related to the pump characteristics. Although it is possible to extract an effective temperature from the linear slope of the logarithmic intensities in a very small energy window ($< 0.1$ eV) near the Fermi level (see Figure S3 in Supplement), this "temperature" does not provide a meaningful description of the photoexcited system. In particular, it fails to account for the actual excess energy in the electronic subsystem due to the spectral features at higher energies. These nonthermal features are even more pronounced for the strong pump. This observation clearly shows that photoexcitation is not the same as heating, and that a full nonequilibrium modeling beyond effective temperature phenomenology is essential for correctly describing pump-probe spectroscopies.

### B. Extracting equilibrium system properties by pump-probe photoemission

As an effective temperature model is inadequate for our purposes, we now focus on a quantitative analysis of energy-dependent relaxation rates for the weaker pump and the higher initial temperature $T = 290$ K. Figure 3a shows the pump-induced spectral changes relative to the initial state, integrated along momenta on the Brillouin zone diagonal, in a continuous map as a function of energy and delay time. Here, the phonon window effect becomes even more obvious: persistent excitations of electrons and holes are only observed inside $\mathcal{W}$, whereas photoexcited electrons outside $\mathcal{W}$ decay on a much faster time scale. The dashed lines mark the phonon window $\mathcal{W}$, which clearly sets the relevant energy scale for slow versus fast relaxation. In Figure 3b, we present cuts for selected energies of the same data as in Figure 3a: Both electrons and holes inside $\mathcal{W}$ decay on a significantly longer time scale than their counterparts outside $\mathcal{W}$. The slight asymmetry between holes and electrons (negative and positive binding energies) is related to asymmetry in the underlying band structure, made clear in the discussion which follows.

We fit decaying exponentials (solid lines in Figure 3b) to these curves starting at a delay time of 250 fs, chosen to be sufficiently large such that pump and probe pulses do not significantly overlap. From these fits we extract the tr-ARPES relaxation rates shown in Figure 4a on a logarithmic scale. The relaxation rates show a steep decline inside the phonon window. This characteristic behavior indeed is reminiscent of the *equilibrium* scattering rates (self-energy) due to coupling between electrons and an optical phonon branch, reflected in a suppression of the imaginary part of the equilibrium self-energy in the phonon window. To make this connection between tr-ARPES relaxation rates and the equilibrium self-energy apparent, we plot $-2\ \mathrm{Im}\ \Sigma_{\mathrm{aver}}$ in Figure 4a. For comparison we account for energy resolution due to the probe pulse width by an additional averaging of relaxation times appropriate for the pump-probe setup (see Supplement).

The good agreement between the tr-ARPES relaxation rates and the equilibrium self-energy suggests that relaxational pump-probe photoemission spectroscopy can be used as an effective tool for accurately measuring equilibrium system properties. Traditionally, equilibrium ARPES experiments are used to extract an estimate for electronic lifetimes through the linewidths of momentum distribution curves (MDCs). For optimal energy and momentum resolution and only a single source of decoherence, the full width at half maximum (FWHM) is related to the relaxation rate at the corresponding energy via $\tau^{-1}(\omega) = \mathrm{FWHM}(\omega) v_F / h$, where $v_F$ is the bare Fermi velocity along the corresponding momentum cut and the equation is valid near the Fermi level for a linear band dispersion. In order to compare relaxation rates extracted from MDC widths directly for the same energy resolution as the tr-ARPES decay rates, we extract the MDC widths from a tr-ARPES snapshot using the same probe width as for the pump-probe simulation.

Even in the absence of other line broadening channels such as impurity or electron-electron scattering, the restricted energy resolution due to the temporal width of the probe pulse leads to MDC linewidths which are not in accordance with the corresponding tr-ARPES relaxation rates (see Figure 4a). The MDCs linewidths imply larger rates, which becomes apparent inside $\mathcal{W}$ where the relaxation rates vary strongly with binding energy and the energy resolution therefore has a crucial effect. This demonstrates that pump-probe ARPES in principle allows one to extract the equilibrium electron-phonon scattering rates more accurately than ARPES MDC measurements.

As a consequence, more detailed knowledge about the electron-phonon scattering processes allows us to quantitatively extract the electron-phonon mode coupling strength from a comparison of the tr-ARPES relaxation rates $\Gamma_{\rm tr}(\omega)$ and the self-energy $\Sigma(\omega)$. To this end, we treat our tr-ARPES relaxation rates as "experimental data" and assume that we know the line shape of Im $\Sigma(\omega)$. Within the Migdal approximation to the Holstein model, the relaxation rate is proportional to $g^2$ and of the form $\Gamma(\omega) = g^2\ \phi(\omega)$ (see Supplement). The function $\phi(\omega)$ reflects electron-phonon scattering processes and takes into account the available scattering phase space related to the electronic band structure via the local electronic density of states $N(\omega)$. This is the reason why an asymmetry in the band structure results in an electron-hole asymmetry in the relaxation rates.

The measured tr-ARPES relaxation rates $\Gamma_{\rm tr}$ are naturally convolved with the probe pulse shape and therefore include an additional energy averaging, since there is a tradeoff between time resolution and energy resolution. Therefore we apply an energy averaging procedure to $\phi(\omega)$ (see Supplement), which yields $\phi_{\rm aver}$. The electron-phonon coupling strength is then extracted from $g^2 = \Gamma_{\rm tr}(\omega)/\phi_{\rm aver}(\omega)$. Figure 4b shows this ratio as a function of energy, which serves as an a posteriori estimate of $g^2$ given the numerical simulation data. The extracted mean value including an error estimate from the statistical standard deviation is $g^2 = 0.021 \pm 0.004$ eV$^2$, to be compared with the exact input value $g^2 = 0.02$ eV$^2$. This agreement highlights the fact that a nonequilibrium measurement can serve as an accurate tool for extracting equilibrium system properties, a feat which may be difficult to accomplish by pure equilibrium measurements.

It might seem counterintuitive that a system out of equilibrium relaxes at the equilibrium scattering time scale, determined by the imaginary part of the self-energy, but this result should hold in nearly all systems at long times. This occurs as for small deviations from equilibrium the change of the spectrum is second order in the deviation from equilibrium, while the change of the occupation is first order, primarily due to the change of the distribution function from the equilibrium Fermi-Dirac distribution.[53,54] Hence, the Green functions should be the same as in equilibrium, except for a small change of the distribution function. If the self-energy of the system in equilibrium does not depend too strongly on temperature, then it is weakly dependent on the distribution function, and as a result, we will see the nonequilibrium system relax back to equilibrium at the longer time scales via the equilibrium relaxation rates.

## II. DISCUSSION

The central result of this paper is that equilibrium ideas can be used to understand the nonequilibrium dynamics of a pumped system. This is facilitated by the connection between relaxation rates for the decay of photoexcited electrons and the equilibrium electron-phonon scattering rates. Importantly, both the dependence of the rates on the binding energy and on the initial equilibrium temperature affect the result, but not the conclusion. We have shown that a simplified modeling in terms of effective temperatures does not provide an adequate description of photoexcited systems with full nonequilibrium quantum dynamics. However, the relation between the equilibrium self-energy and the nonequilibrium relaxation makes pump-probe spectroscopies a convenient tool to disentangle equilibrium decoherence pathways. As a consequence, the strength of electron-phonon couplings can be extracted from pump-probe relaxation times with a high level of accuracy. In addition, our approach also can be applied to general electron-boson interactions, for instance coupling to magnons. It could therefore potentially be used to better characterize the bosonic couplings in high-temperature superconductors.

## III. METHODS

We solve a set of integro-differential equations[55] along the time contour in order to account for electron-phonon interaction effects via a double time self-energy, which dresses the noninteracting Green function. The electric field of the pump pulse is included via a standard Peierls substitution. The code is parallelized easily since the equations for different momentum points decouple in the discretized Brillouin zone. An additional Fourier transform of the lesser component of the resulting interacting Green function is performed to extract the tr-ARPES spectra.[56] In this step, a shape function is introduced to take the probe pulse width into account. Additionally, the momenta need to be time-shifted depending on the pump field to ensure gauge invariance.[57] The details of the formalism are presented in the Supplement.

## ACKNOWLEDGMENTS

We acknowledge discussions with Jonathan Sobota, Inna Vishik, Shuolong Yang, Uwe Bovensiepen, Patrick Kirchmann, Alessandra Lanzara, and Martin Wolf. This work was supported by the Department of Energy, Office of Basic Energy Sciences, Division of Materials Sciences and Engineering (DMSE) under Contract Nos. DE-AC02-76SF00515 (Stanford/SIMES), DE-FG02-08ER46542 (Georgetown), and DE-SC0007091 (for the collaboration). Computational resources were provided by the National Energy Research Scientific Computing Center supported by the Department of Energy, Office of Science, under Contract No. DE- AC02-05CH11231. J.K.F. was supported by the McDevitt bequest at Georgetown.

---

[1] McMillan, W. L. & Rowell, J. M. Lead phonon spectrum calculated from superconducting density of states. *Phys. Rev. Lett.* **14**, 108–112 (1965). URL `http://link.aps.org/doi/10.1103/PhysRevLett.14.108`.

[2] Marsiglio, F. & Carbotte, J. On scattering rates extracted from the optical conductivity. *Can. J. Phys* **75**, 509 (1997).

[3] Marsiglio, F. Implications of reflectance measurements on the mechanism for superconductivity in mgb$_2$. *Phys. Rev. Lett.* **87**, 247001 (2001). URL `http://link.aps.org/doi/10.1103/PhysRevLett.87.247001`.

[4] Knigavko, A., Carbotte, J. P. & Marsiglio, F. Observation of phonon structure in electron density of states of a normal metal. *EPL (Europhysics Letters)* **71**, 776 (2005). URL `http://stacks.iop.org/0295-5075/71/i=5/a=776`.

[5] Ament, L. J. P., van Veenendaal, M. & van den Brink, J. Determining the electron-phonon coupling strength from resonant inelastic x-ray scattering at transition metal l-edges. *EPL (Europhysics Letters)* **95**, 27008 (2011). URL `http://stacks.iop.org/0295-5075/95/i=2/a=27008`.

[6] Devereaux, T. P. & Hackl, R. Inelastic light scattering from correlated electrons. *Rev. Mod. Phys.* **79**, 175–233 (2007). URL `http://link.aps.org/doi/10.1103/RevModPhys.79.175`.

[7] Pintschovius, L. Electron–phonon coupling effects explored by inelastic neutron scattering. *physica status solidi (b)* **242**, 30–50 (2005). URL `http://dx.doi.org/10.1002/pssb.200404951`.

[8] Damascelli, A., Hussain, Z. & Shen, Z.-X. Angle-resolved photoemission studies of the cuprate superconductors. *Rev. Mod. Phys.* **75**, 473–541 (2003). URL `http://link.aps.org/doi/10.1103/RevModPhys.75.473`.

[9] Cuk, T. *et al.* A review of electron-phonon coupling seen in the high-Tc superconductors by angle-resolved photoemission studies (ARPES). *physica status solidi (b)* **242**, 11–29 (2005). URL `http://dx.doi.org/10.1002/pssb.200404959`.

[10] Bogdanov, P. V. *et al.* Evidence for an energy scale for quasiparticle dispersion in $\mathrm{bi_2sr_2cacu_2o_8}$. *Phys. Rev. Lett.* **85**, 2581–2584 (2000). URL `http://link.aps.org/doi/10.1103/PhysRevLett.85.2581`.

[11] Johnson, P. D. *et al.* Doping and Temperature Dependence of the Mass Enhancement Observed in the Cuprate $\mathrm{Bi_2Sr_2CaCu_2O_{8+\delta}}$. *Phys. Rev. Lett.* **87**, 177007 (2001). URL `http://link.aps.org/doi/10.1103/PhysRevLett.87.177007`.

[12] Lanzara, A. *et al.* Evidence for ubiquitous strong electron-phonon coupling in high-temperature superconductors. *Nature* **412**, 510–514 (2001). URL `http://dx.doi.org/10.1038/35087518`.

[13] Kaminski, A. *et al.* Renormalization of Spectral Line Shape and Dispersion below $T_c$ in $\mathrm{Bi_2Sr_2CaCu_2O_{8+\delta}}$. *Phys. Rev. Lett.* **86**, 1070–1073 (2001). URL `http://link.aps.org/doi/10.1103/PhysRevLett.86.1070`.

[14] Dessau, D. S. *et al.* Anomalous spectral weight transfer at the superconducting transition of $\mathrm{Bi_2Sr_2CaCu_2O_{8+\delta}}$. *Phys. Rev. Lett.* **66**, 2160–2163 (1991). URL `http://link.aps.org/doi/10.1103/PhysRevLett.66.2160`.

[15] Cuk, T. *et al.* Coupling of the $B_{1g}$ Phonon to the Antinodal Electronic States of $\mathrm{Bi_2Sr_2Ca_{0.92}Y_{0.08}Cu_2O_{8+\delta}}$. *Phys. Rev. Lett.* **93**, 117003 (2004). URL `http://link.aps.org/doi/10.1103/PhysRevLett.93.117003`.

[16] Gromko, A. D. *et al.* Mass-renormalized electronic excitations at $(\pi, 0)$ in the superconducting state of $\mathrm{Bi_2Sr_2CaCu_2O_{8+\delta}}$. *Phys. Rev. B* **68**, 174520 (2003). URL `http://link.aps.org/doi/10.1103/PhysRevB.68.174520`.

[17] Kim, T. K. *et al.* Doping Dependence of the Mass Enhancement in $\mathrm{(Pb,Bi)_2Sr_2CaCu_2O_8}$ at the Antinodal Point in the Superconducting and Normal States. *Phys. Rev. Lett.* **91**, 167002 (2003). URL `http://link.aps.org/doi/10.1103/PhysRevLett.91.167002`.

[18] Sato, T. *et al.* Observation of band renormalization effects in hole-doped high-$T_c$ superconductors. *Phys. Rev. Lett.* **91**, 157003 (2003). URL `http://link.aps.org/doi/10.1103/`

`PhysRevLett.91.157003`.

[19] Norman, M. R. *et al.* Unusual Dispersion and Line Shape of the Superconducting State Spectra of $Bi_2Sr_2CaCu_2O_{8+\delta}$. *Phys. Rev. Lett.* **79**, 3506–3509 (1997). URL `http://link.aps.org/doi/10.1103/PhysRevLett.79.3506`.

[20] Borisenko, S. V. *et al.* Kinks, Nodal Bilayer Splitting, and Interband Scattering in $YBa_2Cu_3O_{6+x}$. *Phys. Rev. Lett.* **96**, 117004 (2006). URL `http://link.aps.org/doi/10.1103/PhysRevLett.96.117004`.

[21] Borisenko, S. V. *et al.* Parity of the Pairing Bosons in a High-Temperature Pb-$Bi_2Sr_2CaCu_2O_8$ Bilayer Superconductor by Angle-Resolved Photoemission Spectroscopy. *Phys. Rev. Lett.* **96**, 067001 (2006). URL `http://link.aps.org/doi/10.1103/PhysRevLett.96.067001`.

[22] Kordyuk, A. A. *et al.* Constituents of the quasiparticle spectrum along the nodal direction of high-$T_c$ cuprates. *Phys. Rev. Lett.* **97**, 017002 (2006). URL `http://link.aps.org/doi/10.1103/PhysRevLett.97.017002`.

[23] Meevasana, W. *et al.* Doping Dependence of the Coupling of Electrons to Bosonic Modes in the Single-Layer High-Temperature $Bi_2Sr_2CuO_6$ Superconductor. *Phys. Rev. Lett.* **96**, 157003 (2006). URL `http://link.aps.org/doi/10.1103/PhysRevLett.96.157003`.

[24] Zhou, X. J. *et al.* Multiple Bosonic Mode Coupling in the Electron Self-Energy of $(La_{2-x}Sr_x)CuO_4$. *Phys. Rev. Lett.* **95**, 117001 (2005). URL `http://link.aps.org/doi/10.1103/PhysRevLett.95.117001`.

[25] Dahm, T. *et al.* Strength of the spin-fluctuation-mediated pairing interaction in a high-temperature superconductor. *Nat Phys* **5**, 217–221 (2009). URL `http://dx.doi.org/10.1038/nphys1180`.

[26] Valla, T. *et al.* Evidence for Quantum Critical Behavior in the Optimally Doped Cuprate $Bi_2Sr_2CaCu_2O_{8+\delta}$. *Science* **285**, 2110–2113 (1999). URL `http://www.sciencemag.org/content/285/5436/2110.abstract`. http://www.sciencemag.org/content/285/5436/2110.full.pdf.

[27] Allen, P. B. Theory of thermal relaxation of electrons in metals. *Phys. Rev. Lett.* **59**, 1460–1463 (1987). URL `http://link.aps.org/doi/10.1103/PhysRevLett.59.1460`.

[28] Brorson, S. D. *et al.* Femtosecond room-temperature measurement of the electron-phonon coupling constant $\gamma$ in metallic superconductors. *Phys. Rev. Lett.* **64**, 2172–2175 (1990). URL `http://link.aps.org/doi/10.1103/PhysRevLett.64.2172`.

[29] Bovensiepen, U. Coherent and incoherent excitations of the gd(0001) surface on ultrafast timescales. *Journal of Physics: Condensed Matter* **19**, 083201 (2007). URL `http://stacks.iop.org/0953-8984/19/i=8/a=083201`.

[30] Perfetti, L. *et al.* Ultrafast Electron Relaxation in Superconducting $Bi_2Sr_2CaCu_2O_{8+\delta}$ by Time-Resolved Photoelectron Spectroscopy. *Phys. Rev. Lett.* **99**, 197001 (2007). URL `http://link.aps.org/doi/10.1103/PhysRevLett.99.197001`.

[31] Cortés, R. *et al.* Momentum-Resolved Ultrafast Electron Dynamics in Superconducting $Bi_2Sr_2CaCu_2O_{8+\delta}$. *Phys. Rev. Lett.* **107**, 097002 (2011). URL `http://link.aps.org/doi/10.1103/PhysRevLett.107.097002`.

[32] Graf, J. *et al.* Nodal quasiparticle meltdown in ultrahigh-resolution pump–probe angle-resolved photoemission. *Nature Phys.* **7**, 805 (2011).

[33] Rettig, L. *et al.* Ultrafast momentum-dependent response of electrons in antiferromagnetic $eufe_2as_2$ driven by optical excitation. *Phys. Rev. Lett.* **108**, 097002 (2012). URL `http://link.aps.org/doi/10.1103/PhysRevLett.108.097002`.

[34] Kemper, A. F. *et al.* Anisotropic quasiparticle lifetimes in fe-based superconductors. *Phys. Rev. B* **83**, 184516 (2011). URL `http://link.aps.org/doi/10.1103/PhysRevB.83.184516`.

[35] Devereaux, T. P., Cuk, T., Shen, Z.-X. & Nagaosa, N. Anisotropic electron-phonon interaction in the cuprates. *Phys. Rev. Lett.* **93**, 117004 (2004). URL `http://link.aps.org/doi/10.1103/PhysRevLett.93.117004`.

[36] Fausti, D. *et al.* Light-induced superconductivity in a stripe-ordered cuprate. *Science* **331**, 189–191 (2011). URL `http://www.sciencemag.org/content/331/6014/189.abstract`. http://www.sciencemag.org/content/331/6014/189.full.pdf.

[37] Caviglia, A. D. *et al.* Ultrafast strain engineering in complex oxide heterostructures. *Phys. Rev. Lett.* **108**, 136801 (2012). URL `http://link.aps.org/doi/10.1103/PhysRevLett.108.136801`.

[38] Wall, S. *et al.* Ultrafast changes in lattice symmetry probed by coherent phonons. *Nat Commun* **3**, 721 (2012). URL `http://dx.doi.org/10.1038/ncomms1719`.

[39] Hellmann, S. *et al.* Time-domain classification of charge-density-wave insulators. *Nat Commun* **3**, 1069 (2012). URL `http://dx.doi.org/10.1038/ncomms2078`.

[40] Fann, W. S., Storz, R., Tom, H. W. K. & Bokor, J. Direct measurement of nonequilibrium electron-energy distributions in subpicosecond laser-heated gold films. *Phys. Rev. Lett.* **68**,

2834–2837 (1992). URL `http://link.aps.org/doi/10.1103/PhysRevLett.68.2834`.

[41] Schmitt, F. *et al.* Transient Electronic Structure and Melting of a Charge Density Wave in $TbTe_3$. *Science* **321**, 1649–1652 (2008). URL `http://www.sciencemag.org/content/321/5896/1649.abstract`. http://www.sciencemag.org/content/321/5896/1649.full.pdf.

[42] Perfetti, L. *et al.* Time Evolution of the Electronic Structure of 1T-$TaS_2$ through the Insulator-Metal Transition. *Phys. Rev. Lett.* **97**, 067402 (2006).

[43] Perfetti, L. *et al.* Femtosecond dynamics of electronic states in the Mott insulator 1T-$TaS_2$ by time resolved photoelectron spectroscopy. *New J. Phys.* **10**, 053019 (2008).

[44] Sobota, J. A. *et al.* Ultrafast Optical Excitation of a Persistent Surface-State Population in the Topological Insulator $Bi_2Se_3$. *Phys. Rev. Lett.* **108**, 117403 (2012). URL `http://link.aps.org/doi/10.1103/PhysRevLett.108.117403`.

[45] McIver, J. W., Hsieh, D., Steinberg, H., Jarillo-Herrero, P. & Gedik, N. Control over topological insulator photocurrents with light polarization. *Nat Nano* **7**, 96–100 (2012). URL `http://dx.doi.org/10.1038/nnano.2011.214`.

[46] Holstein, T. *Ann. Phys.* **8**, 325 (1959).

[47] Ashcroft, N. W. & Mermin, N. D. *Solid State Physics* (Brooks Cole, 1976).

[48] Jauho, A. P. & Wilkins, J. W. Theory of high-electric-field quantum transport for electron-resonant impurity systems. *Phys. Rev. B* **29**, 1919–1938 (1984). URL `http://link.aps.org/doi/10.1103/PhysRevB.29.1919`.

[49] Tsuji, N., Oka, T., Werner, P. & Aoki, H. Dynamical band flipping in fermionic lattice systems: An ac-field-driven change of the interaction from repulsive to attractive. *Phys. Rev. Lett.* **106**, 236401 (2011). URL `http://link.aps.org/doi/10.1103/PhysRevLett.106.236401`.

[50] Anisimov, S. I., Kapeliovich, B. L. & Perelman, T. L. Electron emission from metal surfaces exposed to ultrashort laser pulses. *Soviet Physics JETP-USSR* **39**, 375 (1974).

[51] Mendez, E. E. & Bastard, G. Wannier-Stark Ladders and Bloch Oscillations in Superlattices. *Physics Today* **6**, 34 (1993).

[52] Moritz, B., Devereaux, T. P. & Freericks, J. K. Time-resolved photoemission of correlated electrons driven out of equilibrium. *Phys. Rev. B* **81**, 165112 (2010). URL `http://link.aps.org/doi/10.1103/PhysRevB.81.165112`.

[53] Mahan, G. D. Quantum transport equation for electric and magnetic fields. *Phys. Rep.* **145**, 251 (1987).

[54] Freericks, J. K. & Turkowski, V. M. Steady-state nonequilibrium dynamical mean-field theory and the quantum boltzmann equation. *Journal of Physics: Conference Series* **35**, 39 (2006). URL `http://stacks.iop.org/1742-6596/35/i=1/a=004`.

[55] Eckstein, M., Kollar, M. & Werner, P. Interaction quench in the hubbard model: Relaxation of the spectral function and the optical conductivity. *Phys. Rev. B* **81**, 115131 (2010). URL `http://link.aps.org/doi/10.1103/PhysRevB.81.115131`.

[56] Freericks, J. K., Krishnamurthy, H. R. & Pruschke, T. Theoretical description of time-resolved photoemission spectroscopy: Application to pump-probe experiments. *Phys. Rev. Lett.* **102**, 136401 (2009). URL `http://link.aps.org/doi/10.1103/PhysRevLett.102.136401`.

[57] Turkowski, V. & Freericks, J. K. *Nonequilibrium dynamical mean-field theory of strongly correlated electrons, in: Strongly Correlated Systems: Coherence and Entanglement* (World Scientific, 2007: 187–210, 2007).

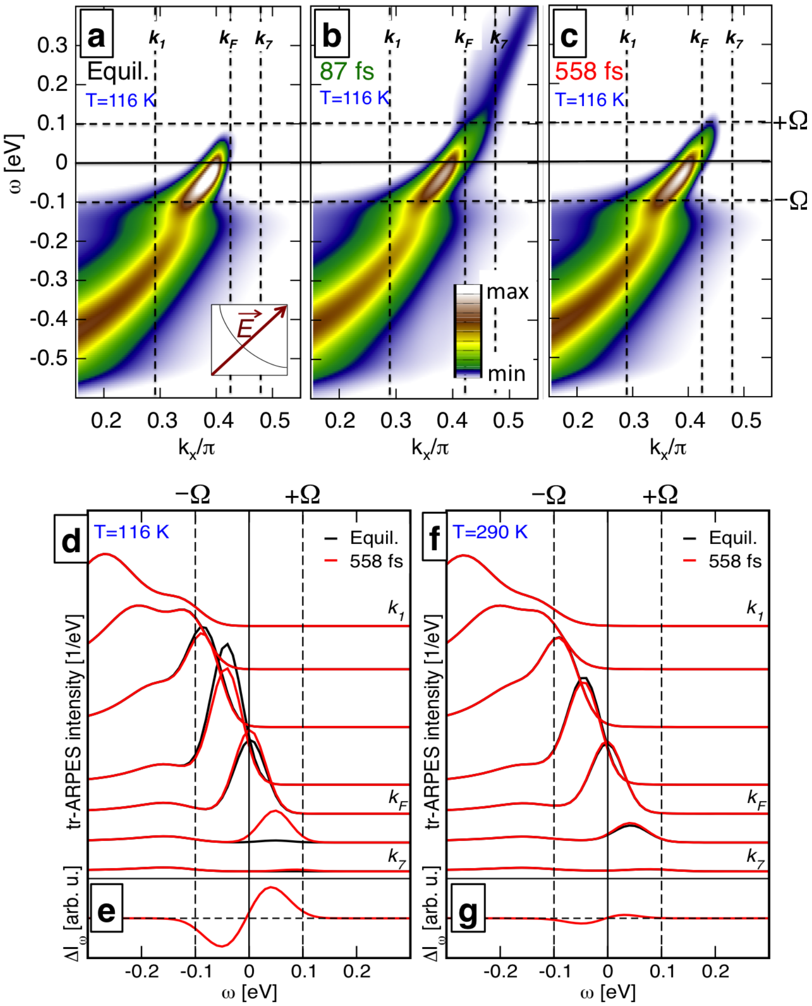

FIG. 1. **$\boldsymbol{k}$-resolved photoexcited electronic structure.** (a) Equilibrium tr-ARPES intensity at temperature $T = 116$ K for a cut along the Brillouin zone diagonal. The pump field polarization is aligned along this direction (inset). Horizontal dashed lines mark the position of "kinks" in the electronic dispersion at $\pm\Omega$. (b) Map of the tr-ARPES intensity shortly (87 fs) after the pump pulse and (c) at a later delay time $t = 558$ fs. The system has partially relaxed toward equilibrium outside the energy range $\pm\Omega$, but quasiparticles remain excited within this range. (d) Energy distribution curves (EDCs) corresponding to the data shown in (a, equilibrium) and (c, 558 fs) for momenta $\boldsymbol{k}_1$ to $\boldsymbol{k}_7$ as indicated in panels (a) and (c). For clarity EDCs are vertically shifted. (e) Intensity difference $\Delta I_\omega$ between photoexcited (558 fs) and equilibrium tr-ARPES data. (f),(g) EDCs and spectral changes (same as in (d),(e)) for a higher initial equilibrium temperature $T = 290$ K, showing that the time for recovery shortens for increased temperature.

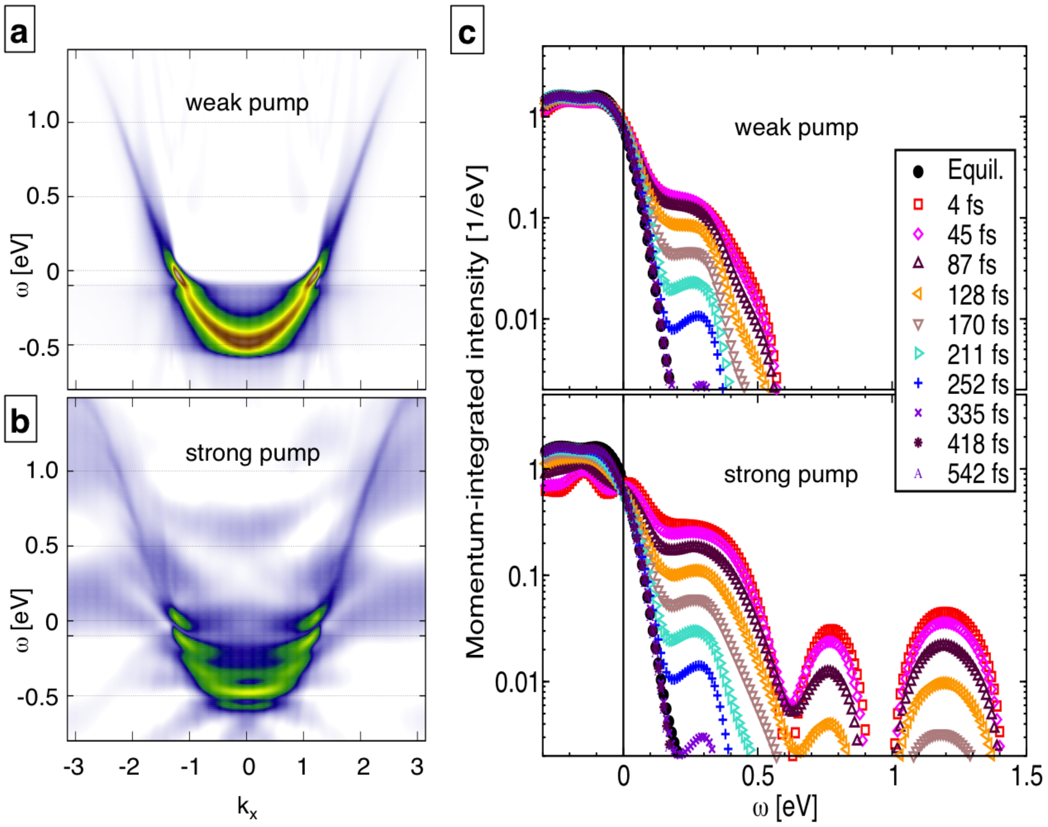

FIG. 2. **Weak versus strong pump field.** **a,** tr-ARPES intensity map (delay time of 4 fs) for a weak pump field (same as in Figure 1) with maximum field strength $E_{\max} = 0.4\ \mathrm{V}/a_0$. **b,** Ten times stronger pump field ($E_{\max} = 4\ \mathrm{V}/a_0$). For a lattice constant $a_0 = 3.4$ Å, these peak field strengths are ≈ 12 MV/cm ("weak pump") and 118 MV/cm ("strong pump"), respectively. **c,** Energy distribution curves integrated over momenta along the Brillouin zone diagonal (same momentum window $\boldsymbol{k}_1$ to $\boldsymbol{k}_7$ close to $\boldsymbol{k}_F$ as indicated in Figure 1) for various pump-probe delay times.

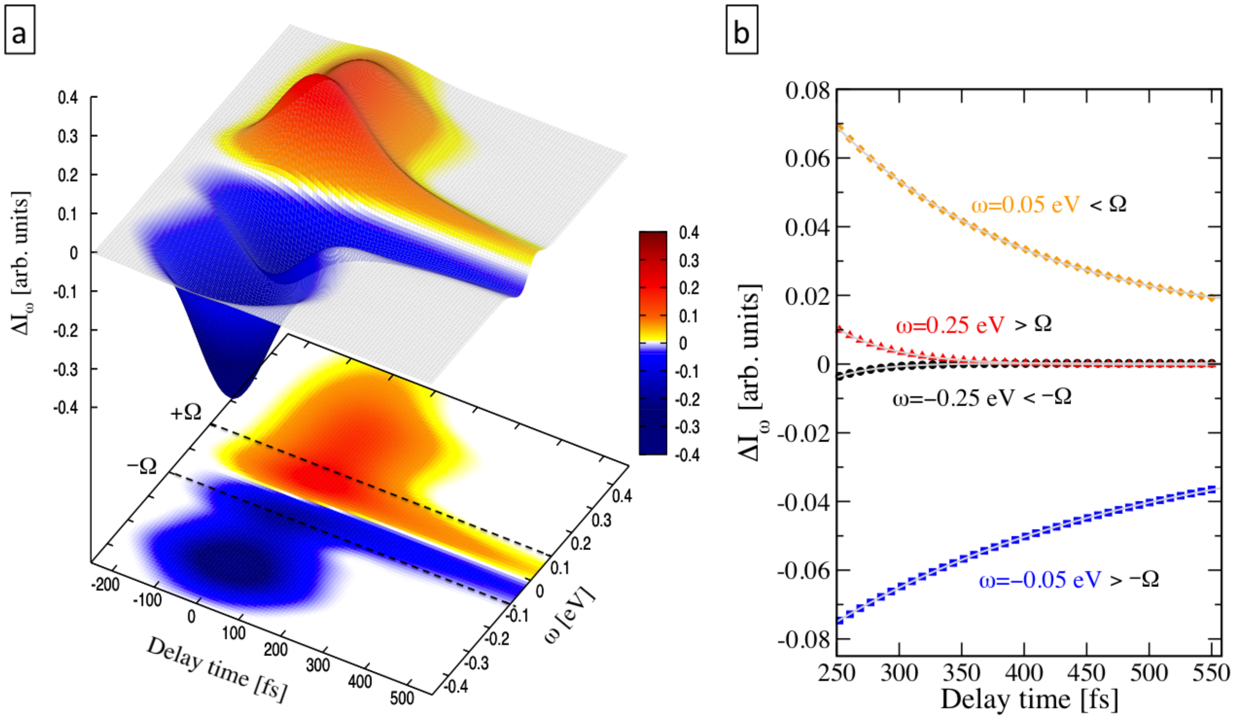

FIG. 3. **Transient relaxation of the pump-induced spectral intensity changes for equilibrium temperature $T = 290$ K.** (a) Spectral changes as a function of pump-probe delay time integrated over momenta along the whole Brillouin zone diagonal. (b) Same data as in **a** for selected energies inside (0.05 eV) and outside (0.25 eV) the phonon window for positive (electrons) and negative (holes) binding energies.

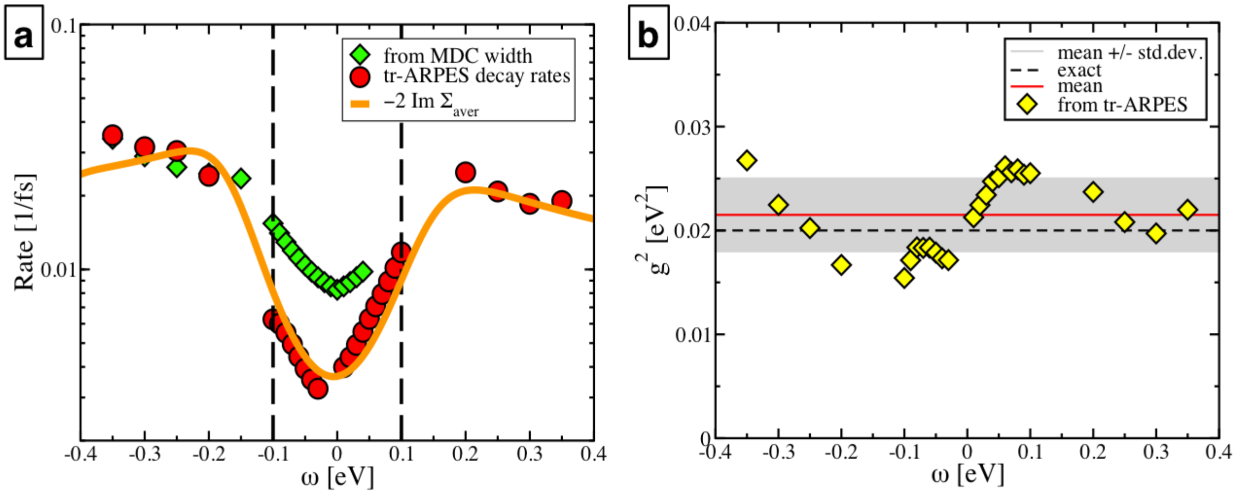

FIG. 4. **Energy dependent relaxation due to electron-phonon scattering.** (a) Relaxation rates from tr-ARPES (red circles) compared with equilibrium MDC widths (green diamonds) for the same probe pulse width. The orange line shows the corresponding equilibrium electron-phonon scattering rate taking into account energy resolution (see Supplement). (b) Extraction of the electron-phonon coupling strength from the ratio of tr-ARPES decay rates and equilibrium self-energy (see Supplement). The red solid line shows the mean value of the data points. The black dashed line indicates the exact input value of $g^2$. The grey shaded area shows the confidence interval estimated from the statistical standard deviation of the data.

arXiv:1212.4841v1 [cond-mat.other] 19 Dec 2012

# Understanding quantum decoherence pathways using time-resolved spectroscopy: Supplementary Material

Michael Sentef, Alexander F. Kemper, Brian Moritz, James K. Freericks, Zhi-Xun Shen, and Thomas P. Devereaux

## S1. FORMALISM

For the formulation of the nonequilibrium problem, we employ the well-established Keldysh Green function technique including the electron-phonon coupling via the electronic self-energy in the Migdal approximation.[1] The double-time Green functions allow us to extract the relevant information (occupation of states, tr-ARPES response) about the excited electron system in a microscopic way. The real and imaginary times involved in the problem define the Keldysh contour shown in Figure S1. The resulting integro-differential equations of motion for the Green functions are solved using massively parallel numerical integration.

We study the Holstein Hamiltonian

$$H = \sum_{\boldsymbol{k}} \epsilon(\boldsymbol{k}) c^\dagger_{\boldsymbol{k}} c_{\boldsymbol{k}} + \Omega \sum_i b^\dagger_i b_i - g \sum_i c^\dagger_i c_i (b_i + b^\dagger_i), \tag{S1}$$

where the individual terms are the electronic kinetic energy with dispersion $\epsilon(\boldsymbol{k})$, the phonon energy for dispersionless Einstein phonons of frequency $\Omega$, and the electron-phonon interaction, respectively. Here $c^{(\dagger)}_{\boldsymbol{k}(i)}$ is the electronic annihilation (creation) operator in momentum space (real space), $b^{(\dagger)}_i$ is the bosonic phonon annihilation (creation) operator on lattice site $i$, and $g$ is the momentum-independent electron-phonon coupling strength.

The driving field is included directly in the propagator via Peierls substitution in the double-time formalism, which leads to the bare non-equilibrium Green function[2]

$$\begin{aligned} G^0_{\boldsymbol{k}}(t,t') =& i \left[ n_F(\epsilon(\boldsymbol{k})) - \theta_c(t,t') \right] \\ & \times \exp \left[ -i \int_{t'}^{t} d\bar{t} \; \epsilon \left( \boldsymbol{k} - \boldsymbol{A}(\bar{t}) \right) \right] \end{aligned} \tag{S2}$$

where $n_F(\omega) = 1/(1 + \exp(\omega/T))$ is the Fermi function at temperature $T$, $t$ and $t'$ are times on the Keldysh contour $\mathcal{C}$, $\theta_c(t,t') = 1$ if $t$ is later on the contour than $t'$ and 0 otherwise, and $\boldsymbol{A}(t)$ is the time-dependent vector potential of the driving field. $\epsilon(\boldsymbol{k})$ is the single-particle energy dispersion for a square lattice with nearest ($V_{nn}$) and next nearest neighbor ($V_{nnn}$) hopping,

$$\epsilon(\boldsymbol{k}) = -2V_{nn} \left( \cos k_x + \cos k_y \right) + 4V_{nnn} \cos k_x \cos k_y - \mu, \tag{S3}$$

measured with respect to the chemical potential $\mu$. In the following we will use a fixed set of model parameters $V_{nn} = 0.25$ eV, $V_{nnn} = 0.075$ eV, $\mu = -0.255$ eV. $\boldsymbol{A}(t)$ is the vector potential at time $t$, which is related to the electric field via $\boldsymbol{A}(t) = -\int^t \boldsymbol{E}(t')dt'$. Here, we use the convention that $\hbar = c = e = 1$, and we work in the Hamiltonian gauge, i.e. the scalar potential is set to zero. Energies are measured in units of eV, time scales in units of h/eV ≈ 4.1 fs.

We incorporate the electron-phonon interactions in the Migdal limit, which is appropriate for weak coupling. In this case the electronic self-energy due to electron-phonon coupling is

$$\Sigma(t,t') = ig^2 \sum_{\boldsymbol{k}} D^0(t,t') G^0_{\boldsymbol{k}}(t,t'). \tag{S4}$$

The bare phonon Green's function $D^0(t,t')$ is[3]

$$\begin{aligned} D^0(t,t') = &- i\left[n_B(\Omega) + 1 - \theta_c(t,t')\right] \exp\left(i\Omega(t-t')\right) \\ &- i\left[n_B(\Omega) + \theta_c(t,t')\right] \exp\left(-i\Omega(t-t')\right) \end{aligned} \tag{S5}$$

where $n_B(\Omega) = 1/(\exp(\Omega/T) - 1)$ is the Bose function.

With the self-energy above, we solve the Dyson equation for the interacting Green function $G$,

$$G_{\boldsymbol{k}}(t,t') = G^0_{\boldsymbol{k}}(t,t') - \int_{\mathcal{C}} dt_1 dt_2 G^0_{\boldsymbol{k}}(t,t_1)\Sigma(t_1,t_2)G_{\boldsymbol{k}}(t_2,t'). \tag{S6}$$

This can be done by casting the Dyson equation as a matrix equation. As an alternative, the Dyson equation can be rewritten by expanding the integral with Langreth rules, which gives equations of motion for the Matsubara, retarded, real-imaginary, and lesser Green's functions.[4,5] This leads to a set of Volterra integro-differential equations that can be solved via standard numerical integration. For the results presented here, we have used the Volterra scheme. Its main advantages are that the equations are manifestly causal, and the required memory is reduced by the use of symmetries.

The external electric pump pulse field is included via a standard Peierls substitution.[6,7] The pulse that is of direct interest to pump-probe experiments is, by nature, a propagating light pulse; this implies an oscillating field without a zero-frequency component. We model the pump via an oscillating vector potential along the (11) or Brillouin zone diagonal direction with a Gaussian profile, where we assume that the field is slowly varying spatially and thus neglect the spatial dependence:

$$\boldsymbol{A}(t) = (\hat{\boldsymbol{x}} + \hat{\boldsymbol{y}})\mathrm{F}_{\max} \sin(\omega_p t) \exp\big(-\frac{(t-t_0)^2}{2\sigma^2}\big). \tag{S7}$$

The tr-ARPES intensity for a probe pulse of width $\sigma_{pr}$ is computed from[8]

$$
\begin{aligned}
I(\boldsymbol{k},\omega,t_0) =& \mathrm{Im}\,\frac{1}{2\pi\sigma_{pr}^2}\int dt\int dt'\tilde{G}^{<}_{\boldsymbol{k}}(t,t') \\
&\times e^{-(t-t_0)^2/2\sigma_{pr}^2}e^{-(t'-t_0)^2/2\sigma_{pr}^2}e^{i\omega(t-t')},
\end{aligned}
\tag{S8}
$$

where the integral is along real times, and each component $\boldsymbol{k}_i$ of the momentum argument of $\tilde{G}^{<}_{\boldsymbol{k}}(t,t')$ is shifted ($\boldsymbol{k}_i \to \boldsymbol{k}_i - \frac{1}{t-t'}\int_t^{t'} d\bar{t}A_i(\bar{t})$, where $A_i$ is the corresponding $i$-th component of the vector potential) to restore gauge invariance.[2]

Figure S2 shows the probe pulse width dependence of tr-ARPES intensity maps and corresponding EDCs, revealing that the necessary energy resolution to resolve the phonon kink and the sharpening of spectral changes to be inside the phonon range has to be achieved by trading off intrinsic time resolution.

## S2. BREAKDOWN OF EFFECTIVE TEMPERATURE DESCRIPTION

Figure S3 shows fits of Fermi functions with effective temperatures and chemical potentials to the low-energy structure of the tr-ARPES energy distribution curves. This figure serves to show that one *can* make such a fit in a small energy window and extract decay constants for the time-dependent temperatures and chemical potentials. However, these do not provide an adequate description of the excited system, which is not at thermal equilibrium. Notably, the time-dependent spectra deviate considerably from the fits already at slightly higher binding energies than the fit window. The figure therefore demonstrates the breakdown of an effective temperature description and calls for a more advanced data analysis. Additionally, we note that even if a Fermi function fit seems to work (see, e.g., Ref. 9), it is easily shown that the extracted decay time for the effective temperature is not related in a simple fashion to energy-dependent decay times for the spectral intensities. This is due to the fact that the intensity at a given binding energy depends nonlinearly on the effective temperature in this case, namely through a Fermi function. Therefore it is doubtful which information can be gained from the temperature decay time.

## S3. RELAXATION RATES

In Figure 1 of the main text, we showed how the relaxation process inside the phonon window is strongly temperature dependent. For low temperatures, the time scales become considerably longer and thus lead to a slower relaxation. Figure S4 shows the corresponding equilibrium relaxation times. Obviously, the times due to electron-phonon scattering are basically independent of temperature outside the phonon window. Inside the phonon window, however, they are strongly temperature dependent. The time scales for our model parameters are well below a picosecond for the higher equilibrium temperature $T$ =290 K, but become as large as tens of picoseconds for $T$ = 116 K.

The relaxation times shown in Figure S4 are obtained from the imaginary part of the equilibrium retarded self-energy according to

$$\tau(\omega) = \frac{-h}{2 \text{ Im } \Sigma^R(\omega)}, \tag{S9}$$

where

$$\begin{aligned} \text{Im } \Sigma^R(\omega) = -\pi g^2 \big[ & N(\omega+\Omega)\,(n_B(\Omega) + n_F(\Omega+\omega)) \\ & + N(\omega-\Omega)\,(n_B(\Omega) + n_F(\Omega-\omega)) \big], \end{aligned} \tag{S10}$$

and $N(\omega) = L^{-1} \sum_{\boldsymbol{k}} \delta(\omega - \epsilon(\boldsymbol{k}))$ (the sum is over the two-dimensional Brillouin zone, with $L$ the number of momentum points summed over) is the bare electronic density of states.[10] The relaxation rate $\Gamma(\omega) = 1/\tau(\omega)$ is thus of the form $g^2\phi(\omega)$, which is used for the extraction of $g^2$ from the tr-ARPES data in the main text. Here, the equilibrium self-energy is taken at the initial temperature of the pump-probe simulation.

For the relaxation rates shown in Figure 4 of the main text, we apply an additional averaging procedure to account for the energy resolution due to the finite width of the probe pulse. The averaged self-energy is obtained by convoluting its inverse with a resolution function:

$$\frac{1}{\text{Im } \Sigma_{\text{aver}}(\omega)} = \int \mathrm{d}\omega' \frac{1}{\sigma_{\text{res}}\sqrt{2\pi}}\, exp \left( \frac{-\omega'^2}{2\sigma_{\text{res}}^2} \right) \frac{1}{\text{Im } \Sigma^R(\omega')}. \tag{S11}$$

For the probe pulse width $\sigma_{pr}$ = 103 fs, the corresponding energy resolution is given by $\sigma_{\text{res}} = \sqrt{2}h/\sigma_{pr} \approx 57$ meV. Note that this is in contrast to Matthiessen's rule for scattering times, which states that inverses of times should be averaged instead of the times themselves. The difference is that Matthiessen's rule applies for averages of scattering processes for various sources of scattering, all for the same particle. Here, however, we are interested in averages of time scales for different particles. The reason why one should average the relaxation times here, instead of the rates, is the following: In the long-time limit, the slowest decaying components determine the effective relaxation rate. To give those components with the longest time scales the largest weight, one has to average times, not rates. The same averaging procedure is applied to yield $\phi_{\mathrm{aver}}$, which is used to extract $g^2$ in Figure 4b of the main text.

Finally, we demonstrate that the relaxation times for particular energies do not significantly depend on the pump field strength as long as one does not measure times too close to the application of the pump. To this end, we show in Figure S5 a comparison of the time scales for exponential fits to the time traces of the energy-dependent tr-ARPES intensities for the weak and strong pumps (see Figure 2 of main text). The times extracted for weak and strong pump pulses agree reasonably well. This overall agreement of the time scales demonstrates that the interpretation of the nonequilibrium dynamics in terms of equilibrium electron-phonon scattering rates is valid even beyond the weak pump regime.

---

[1] Migdal, A. B. *Zh. Eksp. Teor. Fiz.* **34**, 1438 (1958).

[2] Turkowski, V. & Freericks, J. K. *Nonequilibrium dynamical mean-field theory of strongly correlated electrons, in: Strongly Correlated Systems: Coherence and Entanglement* (World Scientific, 2007: 187–210, 2007).

[3] Mahan, G. D. *Many Particle Physics* (Springer, 2010).

[4] Wagner, M. Expansions of nonequilibrium green's functions. *Phys. Rev. B* **44**, 6104–6117 (1991). URL `http://link.aps.org/doi/10.1103/PhysRevB.44.6104`.

[5] Eckstein, M., Kollar, M. & Werner, P. Interaction quench in the hubbard model: Relaxation of the spectral function and the optical conductivity. *Phys. Rev. B* **81**, 115131 (2010). URL `http://link.aps.org/doi/10.1103/PhysRevB.81.115131`.

[6] Peierls, R. *Z. Phys.* **80**, 763 (1933).

[7] Jauho, A. P. & Wilkins, J. W. Theory of high-electric-field quantum transport for electron-resonant impurity systems. *Phys. Rev. B* **29**, 1919–1938 (1984). URL `http://link.aps.org/`

doi/10.1103/PhysRevB.29.1919.

[8] Freericks, J. K., Krishnamurthy, H. R. & Pruschke, T. Theoretical description of time-resolved photoemission spectroscopy: Application to pump-probe experiments. *Phys. Rev. Lett.* **102**, 136401 (2009). URL `http://link.aps.org/doi/10.1103/PhysRevLett.102.136401`.

[9] Crepaldi, A. *et al.* Ultrafast photodoping and effective Fermi-Dirac distribution of the Dirac particles in $Bi_2Se_3$. *Phys. Rev. B* **86**, 205133 (2012). URL `http://link.aps.org/doi/10.1103/PhysRevB.86.205133`.

[10] Cuk, T. *et al.* A review of electron-phonon coupling seen in the high-Tc superconductors by angle-resolved photoemission studies (ARPES). *physica status solidi (b)* **242**, 11–29 (2005). URL `http://dx.doi.org/10.1002/pssb.200404959`.

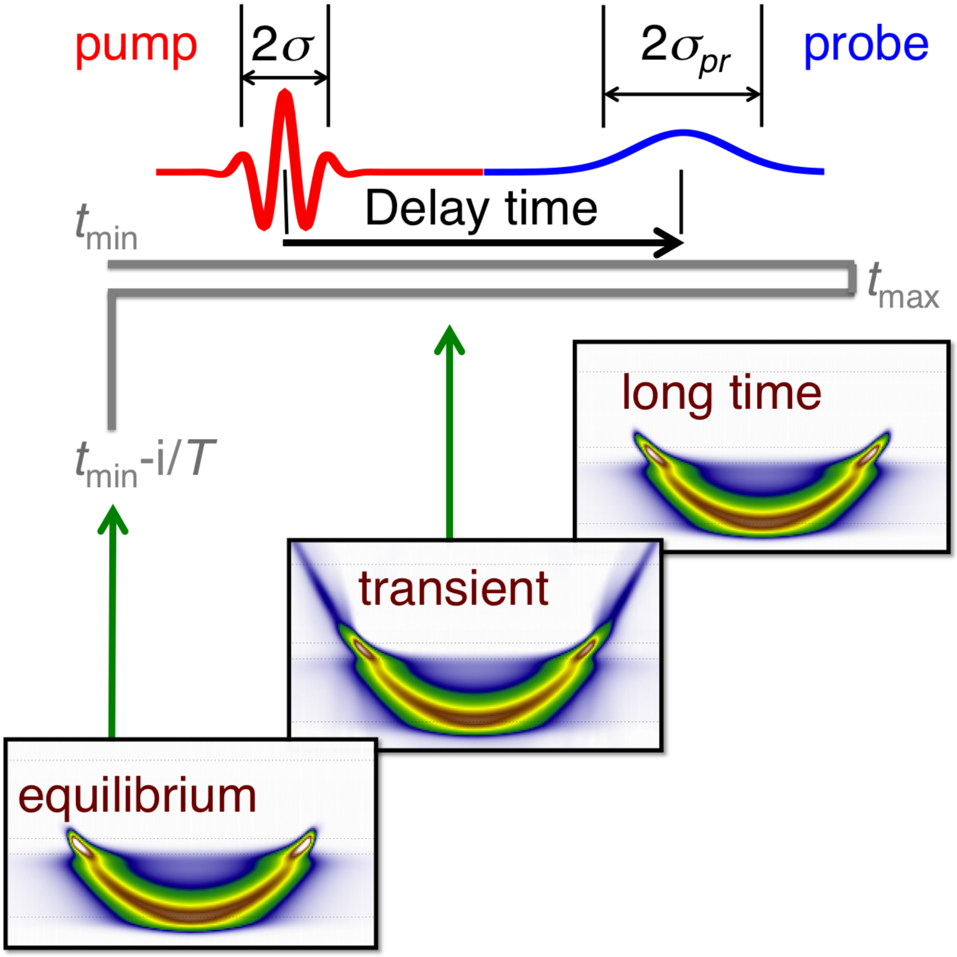

FIG. S1. **Pump-probe photoemission setup with Keldysh contour.** The time-resolved pump-probe photoemission is modeled using nonequilibrium Green functions defined on the Keldysh contour. The contour runs from the initial time $t_{\rm min}$ to a maximum time $t_{\rm max}$ covering the time span of the pump pulse (red) of temporal width $\sigma$ and the probe pulse (blue, only Gaussian envelope shown here) of width $\sigma_{pr}$, then back to $t_{\rm min}$, and from there along the imaginary time direction to $t_{\rm min} - \mathrm{i}/T$. The tr-ARPES snapshots show the electronic structure in equilibrium, in the transient regime at short delay times, and in the long-time limit.

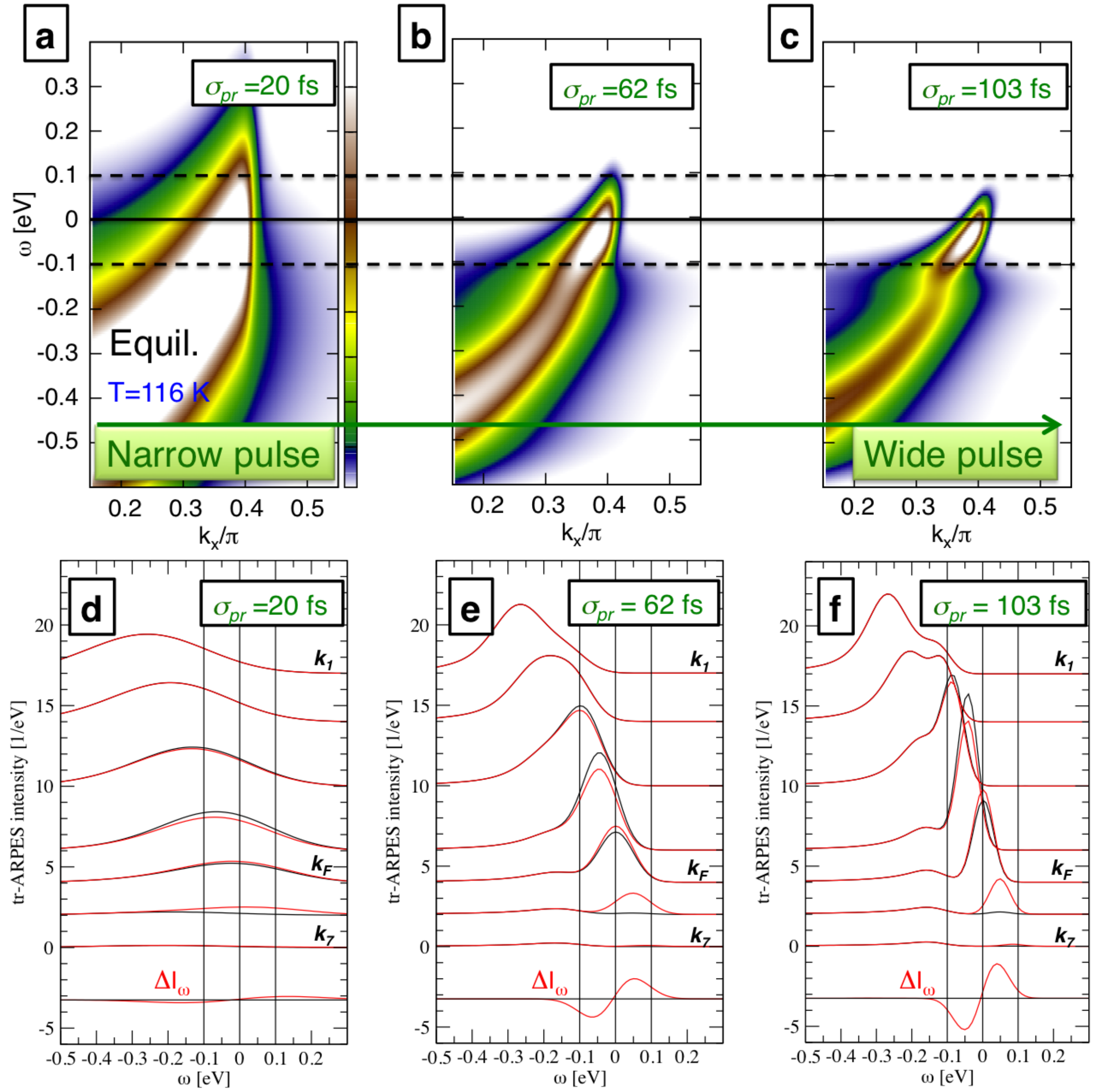

FIG. S2. **Sharpening around phonon edges for increasing energy resolution.** The tr-ARPES signals for various probe pulse widths become sharper for broader probe pulses. At the same time, the restriction of slowly decaying spectral regions to the energy range inside the optical phonon range becomes more apparent.

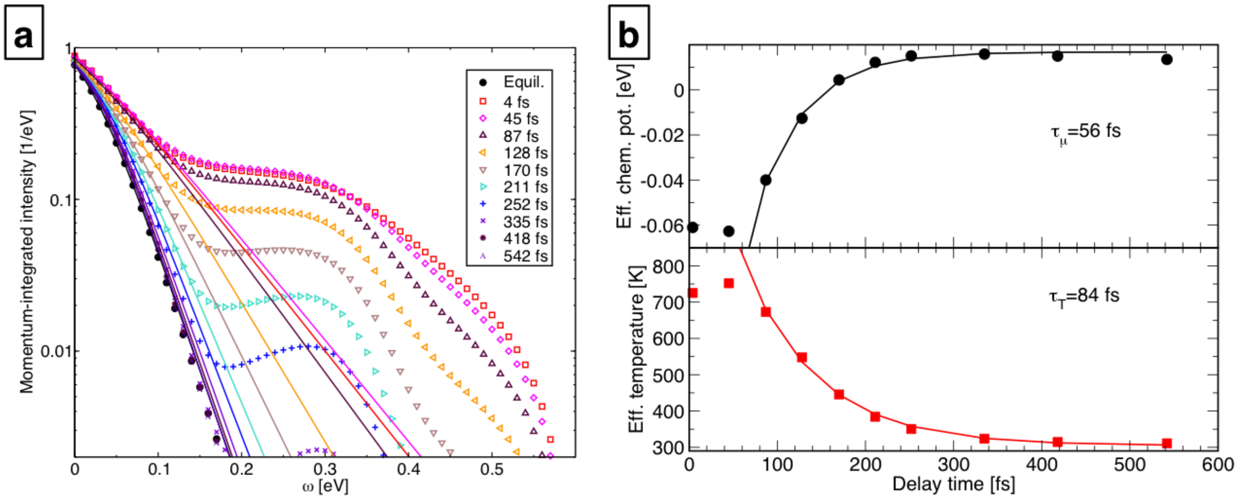

FIG. S3. **Effective temperatures.** (a) Momentum-integrated tr-ARPES data for weak pump (see Figure 2 of main text) with fits to Fermi functions $A/(\exp((\omega - \mu_{\text{eff}}(t))/(k_B T_{\text{eff}}(t))) + 1)$ for time-dependent effective temperatures $T_{\text{eff}}(t)$ and chemical potentials $\mu_{\text{eff}}(t)$. in the energy window between 0 and 0.1 eV. (b) Extracted $\mu_{\text{eff}}(t)$ and $T_{\text{eff}}(t)$ as a function of delay time. The solid lines are fits to decaying exponentials starting at a delay time of 80 fs with decay constants as indicated.

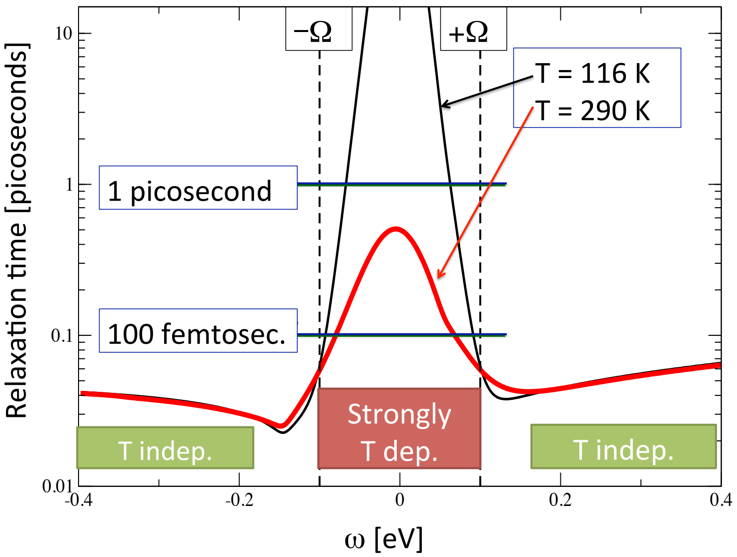

FIG. S4. **Equilibrium temperature dependent relaxation times.** The relaxation times given by the self-energy (without additional frequency broadening) for the two equilibrium temperatures (116 K and 290 K) used in this paper.

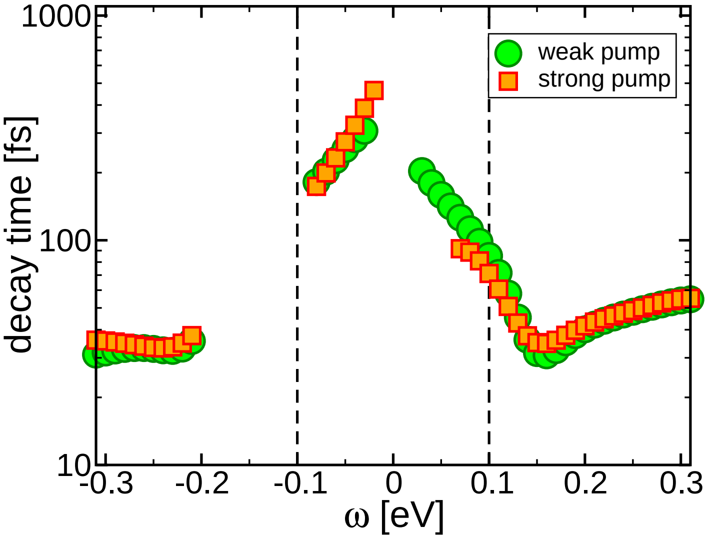

FIG. S5. **Comparison of tr-ARPES relaxation times for weak and strong pumps.** For the weak and strong pump fields (same as in Figure 2 of main text), the energy dependence of tr-ARPES relaxation times is shown here.